Applied Catalysis B: Environmental 183 (2016) 242–253

Contents lists available at ScienceDirect

Applied Catalysis B: Environmental

journal homepage: www.elsevier.com/locate/apcatb

Efficient Co-B-codoped TiO_2 photocatalyst for degradation of organic water pollutant under visible light

R. Jaiswal [a], N. Patel [a,b,*], Alpa Dashora [c], R. Fernandes [a], M. Yadav [a], R. Edla [b], R.S. Varma [a], D.C. Kothari [a], B.L. Ahuja [d], A. Miotello [b]

[a] Department of Physics and National Centre for Nanosciences & Nanotechnology, University of Mumbai, Vidyanagari, Santacruz (E), Mumbai 400 098, India
[b] Dipartimento di Fisica, Università degli Studi di Trento, I-38123 Povo, Trento, Italy
[c] UM-DAE Centre for Excellence in Basic Sciences, Vidyanagari, Santacruz (E), Mumbai 400 098, India
[d] Department of Physics, M.L. Sukhadia University, Udaipur 313 00, India

ARTICLE INFO

Article history:
Received 18 July 2015
Received in revised form 13 October 2015
Accepted 20 October 2015
Available online 11 November 2015

Keywords:
Codoped TiO_2
Photocatalytic activity
Visible light absorption
Sol–gel method
Organic pollutant degradation

ABSTRACT

Lattice location of B in TiO_2 is tuned to determine its effect on the photocatalytic activity of Co-B codoped TiO_2. Sol–gel method was used to synthesize the samples. The concentrations of Co and B were first optimized by maximizing the photocatalytic activity for the monodoped (Co or B)-TiO_2. In addition to the DFT calculations for discovering new energetic levels introduced in TiO_2 by codoping, various characterization techniques were used to determine the dopant lattice sites in TiO_2 and interactions between them; and also determining their consequences on electronic, morphological, structural, and optical properties. At low concentration of B-doping (1 at.%), B occupies the interstitial site (B_{int}), but as the concentration increases (2 at.% and 3 at.%) B also occupies substitutional O position (B_{sub}) in addition to B_{int} to form TiO_2 containing $B_{int+sub}$. Both these B-doped TiO_2 showed improved photocatalytic activity attributed to effective charge separation obtained for TiO_2–B_{int} due to the formation of shallow energy level while higher visible light absorption is achieved with TiO_2–$B_{int+sub}$ owing to the presence of two deep energy levels in the band gap as confirmed by DFT calculations. In the case of Co doping, the band gap of TiO_2 is reduced but the recombination rates are always high and are caused by the formation of Co states in the band gap. For Co monodoped TiO_2, the photocatalytic activity is low for all the concentrations considered, except for very low concentration of Co (0.1 at.%). Two opposite effects were observed when small amount of Co (0.1 at.%) was codoped with B_{int} or $B_{int+sub}$. In particular, the photocatalytic degradation rate of organic aqueous pollutants (*p*-nitrophenol and rhodamine B dye) reduces for TiO_2–Co–B_{int} whereas it is enhanced remarkably for TiO_2–Co–$B_{int+sub}$ as compared to (Co or B) monodoped (~2.1 times) and undoped (~7.8 times) TiO_2. Higher photocatalytic activity observed in Co-doped TiO_2–$B_{int+sub}$ is discussed in terms of the interactions of Co with B at two different lattice positions in TiO_2 and the synergistic effect created by higher visible light absorption and the improved charge separation.

1. Introduction

Photocatalysis, one of the heterogeneous-type advanced oxidation processes (AOPs), is one of the best methods to degrade and eliminate harmful organic pollutants from waste water. Among the various semiconductors studied, TiO_2 is the most promising and extensively studied photocatalyst for eliminating organic pollutants in aqueous or in the gas phase mainly due to its high chemical and thermal stability, environmental friendliness, abundance and cost effectiveness. In addition, the wide range of potential applications of TiO_2 (self cleaning, antibacterial, water splitting, heat exchanger, etc.) makes it an attractive photocatalyst [1]. Unfortunately, TiO_2 shows a wide band gap of 3.2 eV (for anatase phase) thus it utilizes only small fraction of the solar spectrum (~5 % mainly from the UV region) for a photocatalytic reaction. Recombination of photogenerated charges is another major drawback associated with TiO_2. Thus it is of paramount importance to sensitize TiO_2 to absorb major part of the visible light spectrum for generating large number of electron–hole pairs with lowest number of recombinations. Both these issues can be addressed by doping TiO_2 with foreign elements of appropriate concentrations

* Corresponding author at: Department of Physics and National Centre for Nanosciences & Nanotechnology, University of Mumbai, Vidyanagari, Santacruz (E), Mumbai 400 098, India.
E-mail address: nainesh11@gmail.com (N. Patel).

http://dx.doi.org/10.1016/j.apcatb.2015.10.041
0926-3373/

[2–9]. The dopants develop energy levels within the band gap for absorption of significant number of photons and also act as the trapping sites for photogenerated charges to generate optimal charge transfer. Doping with single element (metal or non metal) cannot efficiently serve the purpose because one element forms a single type of defect level either above the valence band (VB) or below the conduction band (CB) in the band gap and creates a small red-shift in the absorption edge of TiO_2 towards the visible part of the spectrum. Besides, these impurity levels can trap only one type of charge carrier either electrons or holes.

Recently, the second generation photocatalysts based on TiO_2 was introduced involving codoping with two different dopant elements, mainly the combination of a metal and a nonmetal. In such a system one element forms defect levels above the VB and the other forms defect levels below the CB to effectively reduce the band gap [10–20]. Additionally, the interaction between the two dopant elements may develop extra hybridization state deep in the band gap which further facilitates in visible light absorption. In addition, these dopants behave as trapping sites for electrons and holes to significantly reduce the recombination processes thus prolonging the charge carrier lifetime. Among nonmetals, N and C are the most investigated as codopants with various metals forming combinations such as Fe–N [12], V–N [13,14], Cu–N [15,16], Cr–N [17], Cr–C [18], Mo–C [19], Fe–C [20] etc.

Among various anions B is the least studied element for codoping with metals cations [21–30]. The behavior of B atoms in TiO_2 is slightly complex mainly related to its position in the lattice and its corresponding photocatalytic activity. In doping, Boron can occupy interstitial and substitutional (replacing oxygen) positions, where B in the former site does not affect the band gap but facilitates in the separation of charges [31–33]. B in the latter case creates intermediate energy levels in the band gap to eventually cause the red shift in the absorption edge without participating in the charge separation [31]. Thus it is necessary to investigate which of the two possible B sites (interstitial or substitutional) will be beneficial for codoping with metal cations. It is also necessary to know, in which way these metal cations will interact with B at different sites to reduce the band gap and the recombination rate, and subsequently enhance the photocatalytic activity. In the past, most of the studies were oriented towards B codoped with N which results in higher visible light photocatalytic activity as compared to single B or N doped TiO_2 [21–23]. Few attempts were also made to co-dope transition metals with B: for example, B–Ni-codoped TiO_2 [25], producing hollow structure, which led to superior photocatalytic activity than its mono-doped and undoped counterparts for NO removal. Similarly, B–Zr–TiO_2 [26], B–V–TiO_2 [27], B–Fe–TiO_2 [28], B–Bi–TiO_2 [29], and B–La–TiO_2 [30] photocatalysts displayed notable performance for degrading organic pollutants. However, none of these reports enlightened the role of the lattice location of B (interstitial or substitutional) in TiO_2 and the interaction of B with metal dopants in improving the photocatalytic activity of B-based codoped photocatalysts.

In the present work, Co and B codoped TiO_2 was synthesized for the first time, to the best of our knowledge, by sol–gel method. Small amount of Co was codoped along with B in two different lattice locations namely: (a) B in interstitial site and (b) B present in both interstitial and substitutional sites. First principles based density functional theory (DFT) calculation with various experimental characterization techniques such as XPS, UV–vis and XRD were used to determine the location of B in TiO_2 and study its interaction with Co. The enhanced photocatalytic activity for the degradation of organic aqueous pollutants obtained with Co-B-codoped TiO_2 is discussed in terms of the interactions of Co with B at two different lattice positions in TiO_2 and the synergistic effect created by the higher visible light absorption and the improved charge separation.

2. Experimental method

Sol–gel method was adopted to synthesize pure, Co-doped, B-doped and (Co,B)-codoped TiO_2 by using titanium butoxide [$Ti(OC_4H_9)_4$], cobalt chloride ($CoCl_2{\cdot}6H_2O$), and boric acid (H_3BO_3) as a Ti, Co and B precursor respectively. To prepare pure TiO_2, $Ti(OC_4H_9)_4$ was first mixed with ethanol and stirred for 1 h. Later mixture of ethanol, H_2O and nitric acid (HNO_3) was added drop wise to the Ti precursor and stirred for 1 h to form homogeneous solution. Molar ratio of $Ti(OC_4H_9)_4/H_2O$/ethanol/HNO_3 was kept constant at 1/30/20/0.1. To synthesize Co-doped TiO_2 hydrated cobalt chloride was mixed with the precursor, while for B-doped TiO_2 boric acid was dissolved in water based solution. Procedure used for Co and B doping was combined to synthesize (Co,B)-codoped TiO_2. Three concentrations of Co (0.1, 0.25, and 0.5 at.%) and B (1, 2, and 3 at.%) doping were used for preparing monodoped TiO_2. Final solution was aged for 24 h at room temperature. The resulting gel was subsequently centrifuged and washed with water and ethanol for several times before drying at 120 °C for 3 h to remove excess solvent. For crystallization all the TiO_2 powder samples were calcinated at 400 °C for 2 h.

The structural characterization was performed by X-ray diffraction (XRD) (Rigaku Ultima IV) using Cu Kα radiation (λ = 1.5414 Å) and by Raman spectroscopy (Renishaw micro-Raman spectrometer (RE-04)) using solid state laser with the diode pumped at 514 nm. The band gap of the doped TiO_2 was determined by measuring diffuse reflectance absorption spectra, using Cary 500 UV–vis-NIR spectrophotometer, in the range of 200–800 nm. The surface composition and chemical states of each element in the samples were examined by X-ray photoelectron spectra (XPS) using a PHI 5000 Versa Probe II instrument equipped with a monochromatic Al Kα (1486.6 eV) X-ray source and a hemispherical analyzer. Appropriate electrical charge compensation was employed to perform the analysis and binding energy was referenced to the C 1s peak. Scanning Electron Microscope (SEM-FEG, JSM 7001F, JEOL) equipped with Energy-Dispersive Spectroscopy analysis (EDS, INCA PentaFET-x3) was used to study the surface morphology and composition of all the samples. Photoluminescence (PL) emission spectra were collected, by exciting the photocatalyst with wavelength of 385 nm, using Fluorescence Spectrophotometer (Varian; Cary Eclipse). Time-resolved photoluminescence spectroscopy (TRPS) was performed using ISS Chronos BH fluorometer. For excitation, pulse diode laser (Hamamatsu) of wavelength 405 nm with pulse width of 70 ps operating with a peak power of 100 mW was used. Both normal and time-resolved PL spectra were acquired by dispersing 3 mg of powder photocatalyst in aqueous medium of fixed amount and transferred into 1 cm × 1 cm cuvette for measurement. The instrument response function was measured with glycogen in water as a scatterer, and multi-exponential curve fitting was done with the Vinci Analysis software. BET surface area of the powder photocatalysts was determined by N_2 absorption at 77 K (Smart SORB 93) after degassing at 120 °C for 2 h.

The photodegradations of two organic water pollutants namely: (a) colorless *p*-nitrophenol (*p*-NP) and (b) colored rhodamine B (RhB) dye solution were carried out to investigate the photocatalytic activity of all the samples under light irradiation. The concentration of pollutant was kept constant at 10 mg/L. 150 W Xenon lamp (Hamamatsu) was used as the source of light having a spectrum nearly similar to solar spectrum. During each photocatalytic degradation experiment, 20 mg of photocatalyst was dispersed in 50 mL of aqueous *p*-NP or RhB solution and stirred for 30 min in dark to attain adsorption-desorption equilibrium of the molecules in the solution. The distance between the beaker and the light source was kept constant at 47 cm. The light fluence was measured to be 5 mW/cm^2 in the reaction solution. After fixed time intervals, 1 mL of *p*-NP or RhB aqueous solution was filtered out

from the reactor vessel and transferred to the 1 cm × 1 cm quartz cuvette. The photocatalytic activity was determined by measuring the normalized intensity of the absorption band of *p*-NP at 320 nm and of RhB at 550 nm using UV–vis spectrophotometer, and plotting it as a function of irradiation time. All the photocatalysis experiments were performed at room temperature and the pH of the solution was maintained neutral during all the photocatalytic measurements.

2.1. Theoretical calculations

To understand the detailed electronic structure and effect of Co and B atoms at different sites in TiO_2 lattice, we have performed DFT based calculations as embodied in WIEN2k code [34]. This code is based on the full-potential linearised augmented plane wave (FP-LAPW) prescription. In FP-LAPW prescription, wave functions, charge density, and potential are expanded in spherical harmonics within non-overlapping muffin-tin (MT) spheres, while plane waves are used in the remaining interstitial region of the unit cell. Core and valence states are, respectively, treated within a multi-configuration relativistic Dirac–Fock approach and scalar relativistically. The exchange and correlation within the generalized gradient approximation [35] with modified Backe–Johnson (mBJ) [36] correction were used. For pure anatase TiO_2, lattice parameters were considered as $a = 3.838$ and $c = 9.642$ Å as optimized by Rubio-Ponce et al. [37] using FP-LAPW scheme.

In the present calculations, we have considered the interstitial and combination of interstitial and substitutional (at O-site) sites for B, and substitution (at Ti site) for Co in TiO_2, referred in the text as TiO_2–B_{int}, TiO_2–$B_{int+sub}$ and TiO_2–Co, respectively. The effect of codoping of Co and B is also checked with considering: (1) Co at substitutional site and B at interstitial site [TiO_2–Co–B_{int}], and (2) Co at substitutional site with B at interstitial and substitutional sites [TiO_2–Co–$B_{int+sub}$]. In addition to this, we have also considered B at substitutional site, but due to its very high formation energy, higher than TiO_2–B_{int} and TiO_2–$B_{int+sub}$, results are not shown here.

For the present computations, radii for MT spheres were selected as 1.92 a.u. for Ti and Co, 1.74 a.u. for O and 1.62 a.u. for B atom. The ***k***-point sampling of the Brillouin zone (BZ) was set $14 \times 14 \times 14$ and $5 \times 5 \times 5$ for pure TiO_2 and other studied compounds, respectively. Other computational parameters were set as $R_{MT}K_{max} = 7$, $l_{max} = 10$ and $G_{max} = 12$ [34]. Finally all the structures were fully relaxed for atomic forces until the forces on each atom reach a value less than 5 mRy per a.u. To ensure sufficient accuracy in convergence, total energy of all the studied compounds was converged to 0.01 mRy.

3. Results and discussion

TiO_2 was monodoped with Co or B with three different concentrations in order to select the optimum concentration for codoping. Low concentration of 0.1, 0.25, and 0.5 at.% was used to dope Co while the amount of B doping was around 1, 2, and 3 at.% in TiO_2. The range of selected values was chosen so as to limit the deterioration in photoactivity due to recombination of photogenerated charges, as it is well known that at high concentrations the same dopants behave as recombination sites. Fig. 1 presents the XRD pattern of B-doped and Co-doped TiO_2. In pure TiO_2 all the diffraction peaks (25.3°, 37.7°, 48.1°, 53.8° and 55.1°) were indexed to the anatase phase of TiO_2. After B (Fig. 1a) or Co doping (Fig. 1b) the peaks due to the rutile phase (27.3°, 36.0°, 39.2°, 41.2°, 44.0°, and 56.65°) are also visible along with the anatase phase. As the dopant concentration increases, the intensity of the rutile peak increases, thus confirming the presence of dopant inside the TiO_2 lattice which causes the rearrangement of the atoms to promote anatase to rutile

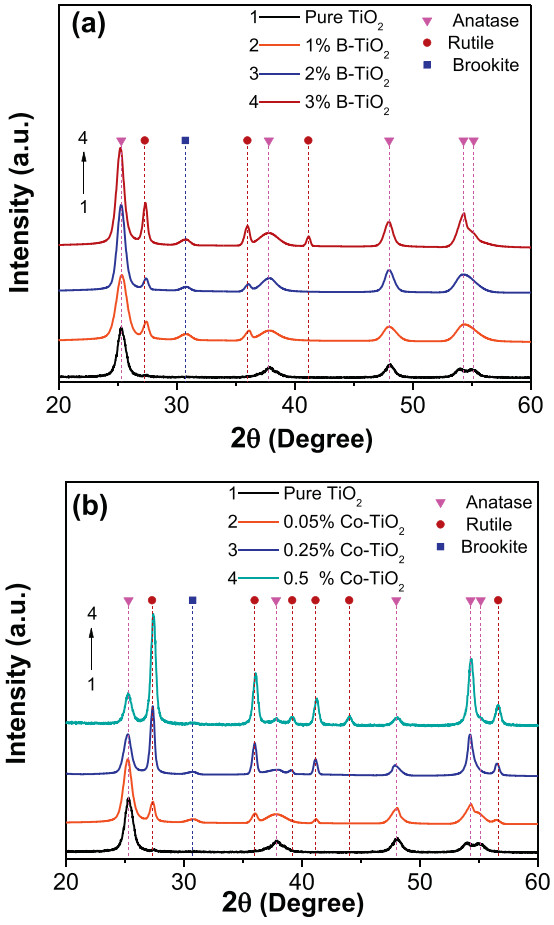

Fig. 1. XRD patterns of (a) B-doped and (b) Co-doped TiO_2 powders with different dopant concentrations.

phase formation. This phenomenon is so effective in Co doping that at concentrations of 0.25 and 0.5 at.% the rutile phase is dominating over the anatase phase (Fig. 1b). Small signal due to the brookite phase (30.8°) is also visible which remains unaffected by increasing dopant concentration. Raman spectroscopy was utilized to study the crystal structure of the photocatalyst surface and the results are presented in Fig. 2. In agreement with the XRD, Raman spectra (Fig. 2) also display the modes of vibrations of only anatase phase for pure TiO_2. The mixture of anatase, rutile and brookite phases for B-doped and Co-doped TiO_2 with major contribution from the anatase phase was also observed in Raman spectra. At higher concentration of Co (0.5 at.%) the rutile phase prevails over the anatase phase (Fig. 2b). The signal due to boron oxide or cobalt oxide is not detected in the XRD pattern as well as in the Raman spectra. The average crystal size was in the range of ~7–12 nm, as calculated from the width of XRD peaks, for all the samples.

The absorption spectra measured in diffuse reflectance mode are reported in Fig. 3 for Co-doped and B-doped TiO_2. As compared to pure TiO_2, the absorption edge is red shifted for the doped TiO_2 irrespective of type and concentration of dopant. In the case of B-doped TiO_2 (Fig. 3a), the shift is low for 1 at.% B-doped TiO_2 while it is maximum for 2 at.% B-doped TiO_2. At the highest concentration of B doping (3 at.%) the absorption edge is again shifted to lower wavelengths (higher energy) as compared to that of 2 at.% B. Nearly the same amount of red shifting in the absorption edge is observed for all the Co-doped TiO_2 samples. The band gap value is determined using Tauc plot and summarized in Table 1. For pure TiO_2 the band gap of 3.15 eV was obtained which is close to the theoretical value of the anatase phase (3.2 eV). Upon low concentration of B-doping,

Table 1
Crystal size (measured from XRD pattern), BET surface area and band gap (obtained from Tauc plot) of pure TiO_2, 1B–TiO_2, 2B–TiO_2, Co–TiO_2, Co–1B–TiO_2 and Co–2B–TiO_2.

Sample name	Crystal size (nm)	Surface area (m^2/g)	Band gap (eV)	
TiO_2	7.9	47	3.15	
1B-TiO_2	11.5	63.1	3.02	
2B-TiO_2	11.0	50.6	2.41	2.20
Co-TiO_2	10.5	60.1	2.32	
Co-1B-TiO_2	7.1	108.1	2.75	
Co-2B-TiO_2	9.3	74.4	2.35	1.91

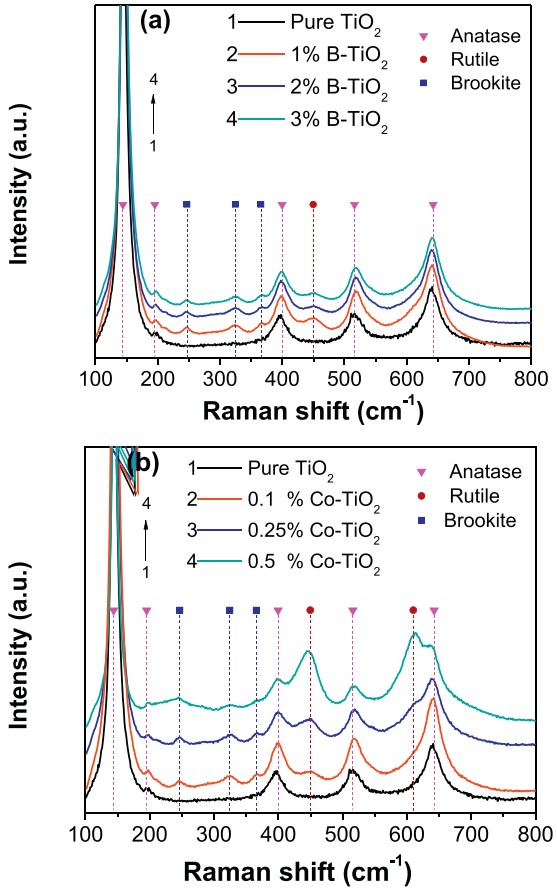

Fig. 2. Raman spectra of (a) B-doped and (b) Co-doped TiO_2 powders with different dopant concentrations.

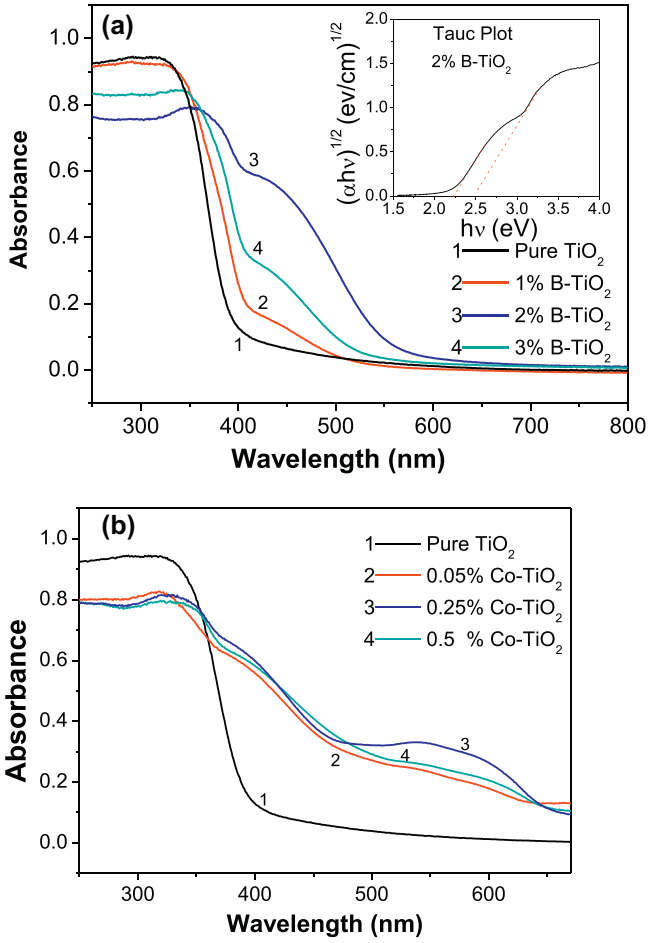

Fig. 3. UV–vis absorption spectra (taken in diffuse reflectance mode) of (a) B-doped and (b) Co-doped TiO_2 powders with different dopant concentrations. Inset of (a) shows the Tauc plot of 2 at.% B-doped TiO_2.

say 1 at.%, the bandgap decreases by small amount to 3 eV. A new energetic feature is observed for 2 at.% B-doping from Tauc plot (inset Fig. 3a) which shows the presence of two absorption edges (2.4 eV and 2.2 eV) suggesting a possible existence of localized state deep in the band gap causing the two step transition. Similar characteristic of the absorption edge is visible for 3 at.% B-doping but with higher energy transition. The reason for this reverse shift in the band edge for 3 at.% B-doped TiO2 is explained in details in our previous work [38]. Briefly, as B concentration increases above 2 at.% the formation of B_2O_3 in noticeable amount is detected by XPS. At higher concentrations, after saturating the interstitial and substitutional sites, the extra boron might contribute in forming B_2O_3 species. This species will also contribute to the absorption edge of TiO_2 and since the band gap of B_2O_3 (6.2 eV) is higher than that of TiO_2, so as the concentration of B increases the absorption edge is blue shifted for B-doped TiO_2 at 3 at.%. The band gap value of about 2.4–2.7 eV is obtained for all the Co-doped TiO_2 catalyst.

The photocatalytic activity of Co-doped and B-doped TiO_2 was tested by studying the degradation of *p*-NP aqueous solution as a function of time. By measuring the relative intensity of the peak at 320 nm in the UV range of optical absorption spectrum, the decrease in *p*-NP concentration was estimated. In the absence of photocatalyst, very low amount of light-induced degradation of *p*-NP was observed after 4 h. All the three B-doped TiO_2 photocatalysts displayed better photocatalytic activity as compared to that of pure TiO_2, with 1 at.% B-doped TiO_2 showing the highest degradation activity. In time period of 4 h, 1 at.% B-doped TiO_2 was able to degrade 75% of *p*-NP with the rate 4 times higher than that of pure TiO_2 which was able to degrade only 20% in the same time interval. However, at higher B concentrations of 2 at.% and 3 at.% the rate decreases but is still higher than that of pure TiO_2. In the case of Co-doped TiO_2, only low concentration Co-doping of 0.1 at.% is effective in enhancing the photocatalytic activity as compared to the pure TiO_2 (Fig. 4). On the other hand, the Co concentrations of 0.25 at.% and 0.5 at.% showed nearly similar degradation rate as that of pure TiO_2.

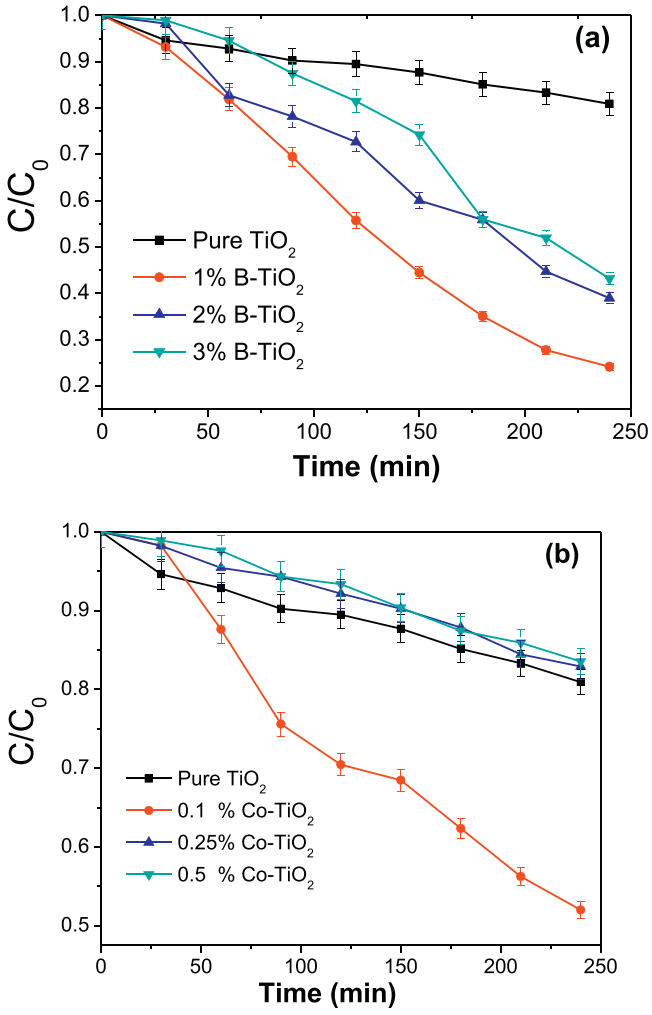

Fig. 4. Comparison of photocatalytic degradation of p-nitrophenol under light irradiation in presence of (a) B-doped and (b) Co-doped TiO_2 powders with different dopant concentrations, plotted in terms of the normalized intensity of the absorption band of *p*-NP at 320 nm in UV–vis spectra vs irradiation time (lines are drawn to guide the eye).

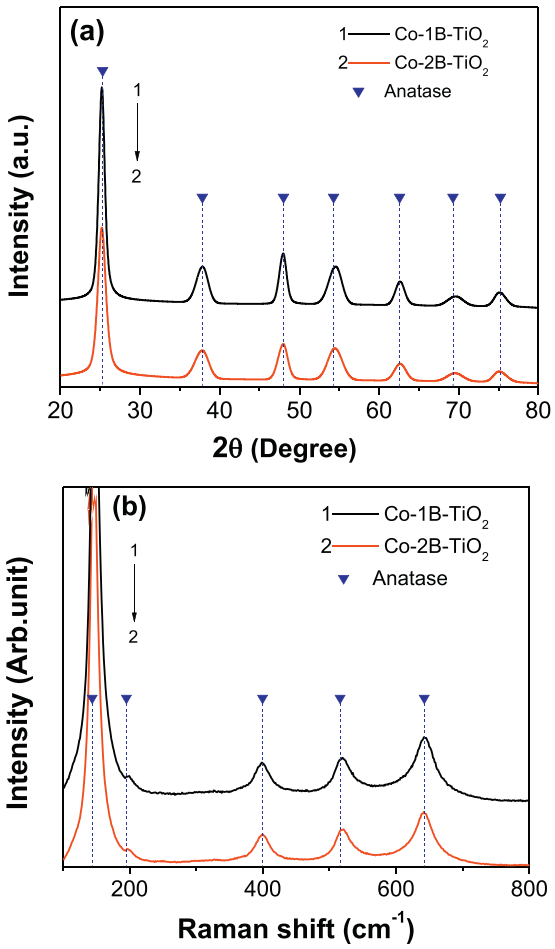

Fig. 5. (a) XRD pattern and (b) Raman spectra of Co–1B–TiO_2 and Co–2B–TiO_2 photocatalysts.

Thus the low concentration Co (0.1 at.%) and B (1 at.%) showed the best photo degradation performance. However, in terms of light absorption, TiO_2 with 2 at.% B doping is significantly active in visible light than 1 at.% B doping and therefore this concentration cannot be neglected. On the basis of these results, for considering Co-B-codoped TiO_2, two samples with the following dopant concentrations were synthesized, (a) Co (0.1 at.%) & B (1 at.%) and (b) Co (0.1 at.%) & B (2 at.%). Henceforth these samples will be designated as Co–1B–TiO_2 and Co–2B–TiO_2 respectively, while monodoped samples with the dopant concentrations of 0.1 at.% Co, 1 at.% B, and 2 at.% B are recognized as Co–TiO_2, 1B–TiO_2, and 2B–TiO_2 respectively.

Further analyses were conducted on only six samples including pure TiO_2, 1B–TiO_2, 2B–TiO_2, Co–TiO_2, Co–1B–TiO_2 and Co–2B–TiO_2. The structural modifications taking place in the bulk and on the surface of TiO_2 due to codoping were studied using XRD (Fig. 5a) and Raman spectroscopy (Fig. 5b), respectively. Unlike single element doped TiO_2, the pure anatase phase is preserved after codoping in both Co–1B–TiO_2 and Co–2B–TiO_2 samples. No signals due to either rutile or brookite phase are present in both XRD patterns and Raman spectra while rutile phase was significantly present in monodoped samples (Co–TiO_2 and B–TiO_2). The anatase to rutile phase transformation is related to the oxygen vacancies formed in the TiO_2 lattice by the inclusion of dopants, depending on the valence state and ionic radius of the dopants [39]. Thus in the present case, the level of oxygen vacancy increases when Co or B are monodoped in TiO_2. On the contrary, when Co and B are codoped, the interaction between both the elements might avoid the formation of oxygen vacancies consequently inhibiting the anatase to rutile phase transformation. The crystallite size, measured using the XRD peak-widths, is about 9 and 7 nm for Co–2B–TiO_2 and Co–1B–TiO_2 respectively. Among all the samples (Table 1), Co–2B–TiO_2 showed the smallest crystallite size. The SEM images of pure TiO_2, 1B–TiO_2, 2B–TiO_2, Co–TiO_2, Co–1B–TiO_2 and Co–2B–TiO_2 powders are shown in Fig. 6a–f respectively. All the photocatalysts showed particle-like morphology with the particle size in the range of 8–15 nm, in good agreement with that obtained from the XRD peaks. Surface area measured by single point BET method using N_2 absorption is reported in Table 1, for all the samples. The surface area increases for all the doped-TiO_2 samples with higher values recorded for the codoped samples, specifically Co–1B–TiO_2 shows highest surface area (108.1 m^2/gm). This result suggests that a dopant plays an important role in avoiding the agglomeration of TiO_2 particles, therefore improving the surface area.

XPS was used to determine the chemical states of each element present in all the six samples. The XPS spectra are reported in Fig. 7. Two peaks centered at 458.4 eV and 464.1 eV assigned to Ti $2p_{3/2}$ and Ti $2p_{1/2}$ states of Ti^{4+} are visible in XPS Ti 2p core levels spectra of pure TiO_2, 1B–TiO_2, Co–TiO_2 and Co–1B–TiO_2 samples. Similar peaks were detected in the XPS spectra of 2B–TiO_2 and Co–2B–TiO_2

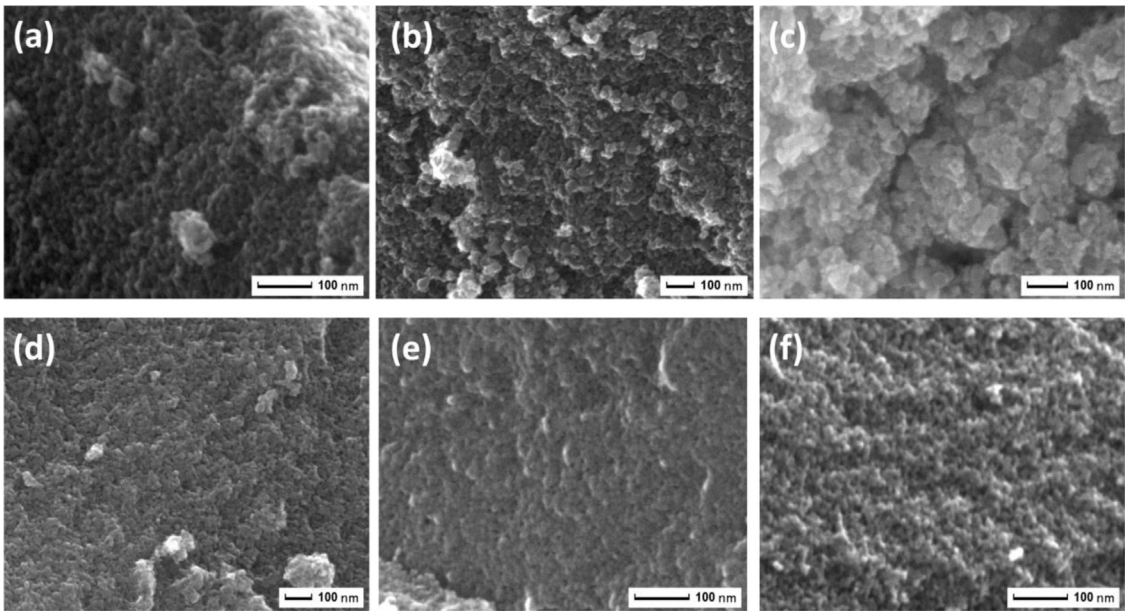

Fig. 6. SEM images of (a) pure TiO_2, (b) 1B–TiO_2, (c) 2B–TiO_2, (d) Co–TiO_2, (e) Co–1B–TiO_2 and (f) Co–2B– TiO_2.

samples, but with positive shift in binding energy (BE) by 0.2 eV. This shift shows that B when present in high concentration in TiO_2 lattice, influences the local chemical states of Ti^{4+} ion. The signal due to Ti^{3+} was detected only on the surface of 1B–TiO_2, which is seen as a shoulder at around 456.8 eV in the XPS spectrum. In the O1s core level XPS spectra of all samples, only single peak centered at 529.8 eV is seen. The deconvolution of this peak suggests that the main signal (529.8 eV) is due to O bonded in TiO_2 with minor traces due to B—O bond and OH group attached on the surface. The analysis of Co 2p core level peak suggests that Co is present mainly in Co^{2+} state of CoO species with a peak centered at 780.8 eV and a satellite peak at 786.4 eV. In all the codoped samples except for Co–2B–TiO_2, small amount of metallic cobalt (778.4 eV peak in XPS spectra) is also present. In the XPS spectra of B 1s core level, a broad peak is observed for 1B–TiO_2 and Co–1B–TiO_2 samples. This peak was deconvoluted into two peaks with BE of 191.7 eV and 193.6 eV attributed to interstitial B and boron oxide (B_2O_3) where the major peak contribution (95%) is due to the former peak. In addition to these two peaks a small peak centered at 189.0 eV assigned to substitutional B at oxygen site was also visible for 2 at.% B doping in both 2B–TiO_2 and Co–2B–TiO_2 powders. Although the major contribution is from interstitial B (70%) the substitutional B is clearly noticeable (25%). These results show that Co is present in the form of Co^{2+} state at the Ti^{4+} lattice site. In the case of low concentration B-doping, B is mainly present at interstitial site to form B—O—Ti bond while as the concentration increases (2 at.%) B is not only present at the interstitial site but also occupies substitutional site by replacing oxygen atom in the lattice. In addition, the separation between the B 1s peak of B_{sub} and B_{int} is about 2.7 eV which is in good agreement with that reported by the calculation (2.6 eV) performed by Finazzi et al. [31]. Most importantly the location sites of B for 1 at.% and 2 at.% B-doping does not change upon codoping with small amount of Co in Co–1B–TiO_2 and Co–2B–TiO_2. Where the former contains only interstitial B and later acquires both interstitial as well as substitutional B.

Absorption spectra of pure TiO_2, monodoped and codoped TiO_2 are reported in Fig. 8. The band gap value, obtained from Tauc plot, of Co–1B–TiO_2 decreases by small amount to 2.75 eV with respect to that of 1B–TiO_2 (3.02 eV). The two step transition is maintained in Co–2B–TiO_2 as found in 2B–TiO_2, with the absorption edge further red shifted to 2.35 eV and 1.91 eV. This shows that even though the concentration of Co doping is very low (0.1 at.%) it considerably affects the bandgap value when added to B-doped TiO_2. Most importantly, the features of absorption edge of B-doped TiO_2 are maintained upon codoping with small amount of Co dopants. The role of dopants in narrowing the bandgap of TiO_2 is discussed in the next section.

Theoretical calculations were carried out using DFT with mBJ potential, in order to precisely correlate the role of dopant species in modifying the electronic structure of TiO_2. According to the above XPS results, when B is present at low concentration (1 at.%) it occupies the interstitial site but as the concentration increases to 2 at.%, B also substitutionally replaces oxygen in addition to the interstitial occupancy. The position of B is maintained in the codoped TiO_2. On the other hand, Co is placed at the Ti site in the lattice. Considering these results, the calculation was performed for single element doped TiO_2 (a) by placing B in the interstitial position (TiO_2–B_{int}), (b) by imposing B at both substitutional as well as interstitial sites (TiO_2–$B_{int+sub}$) and (c) by substitutionally replacing Co at Ti sites. In the case of codoped TiO_2, the combination of (a) with (c), and (b) with (c) were implemented for calculation in order to simulate the Co–1B–TiO_2 and Co–2B–TiO_2 samples refereed as TiO_2–Co– B_{int} and TiO_2–Co–$B_{int+sub}$ respectively.

Fig. 9(a–f) presents energy band diagrams and partial density of states (PDOS) for mono-doped and codoped TiO_2 with B and Co. Fig. 9a shows the energy bands and DOS of pure anatase TiO_2. Our calculations with mBJ potential show that TiO_2 has a direct band gap of 3.2 eV at Γ point and an indirect band gap of 2.9 eV between Γ and Γ–N branch. The value of band gap is in good agreement with the experimental value (within 10%). From the PDOS it is seen that the valence band (VB) of TiO_2 is mainly dominated by O states while the conduction band (CB) is due to the Ti states. In the case of TiO_2–B_{int} (Fig. 9b) Fermi energy (E_F) is shifted towards the CB which shows that the B at interstitial site in TiO_2 works as n-type dopant. Two energy bands near to CB below $\underline{E}_F$ are formed and the band gap is reduced by 0.20 eV from that of pure TiO_2. This narrowing of band gap is in well agreement with that obtained from the UV–vis spectra of 1B–TiO_2 where the absorption edge is red shifted by 0.15 eV due to the interstitial occupancy of B as confirmed by XPS. PDOS shows that the shallow level formed in B_{int} is contributed due to overlapping of three Ti, O and B states. This suggests that strong hybridization occurs between Ti, O and B states to form B—O—Ti

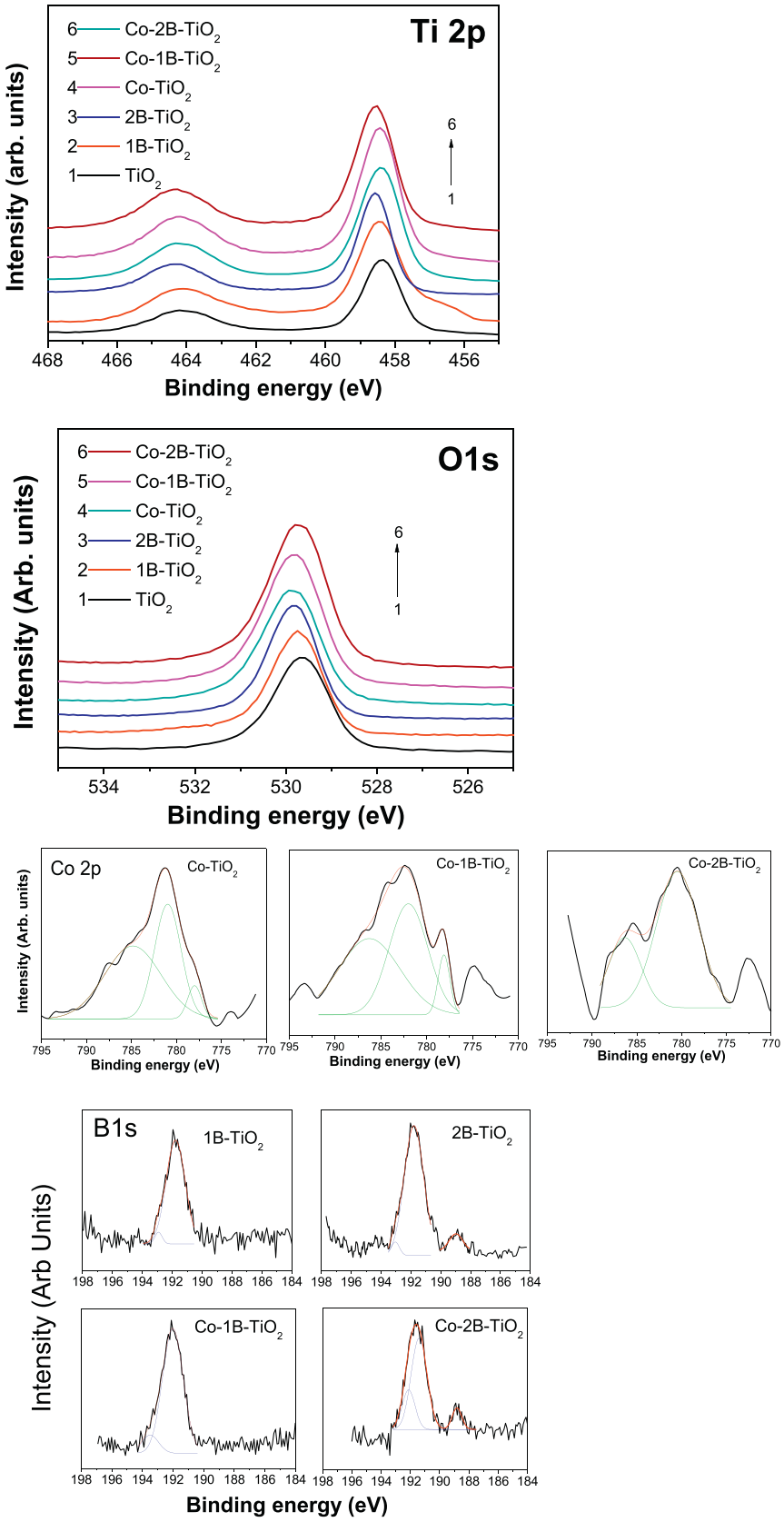

Fig. 7. XPS spectra of Ti2p, O1s, Co2p and B1s levels of pure TiO_2, 1B–TiO_2, 2B–TiO_2, Co–TiO_2, Co–1B–TiO_2 and Co–2B–TiO_2.

bond in the lattice, also confirmed by the XPS result, which is responsible for the slight narrowing of the band gap. When B atoms are placed at both the interstitial and substitutional sites, two localized impurity states due to the substitutional B are formed below the CB deep in the band gap as observed in the energy band diagram (Fig. 9c). At Γ position of BZ, these states are placed at about 2.24 eV

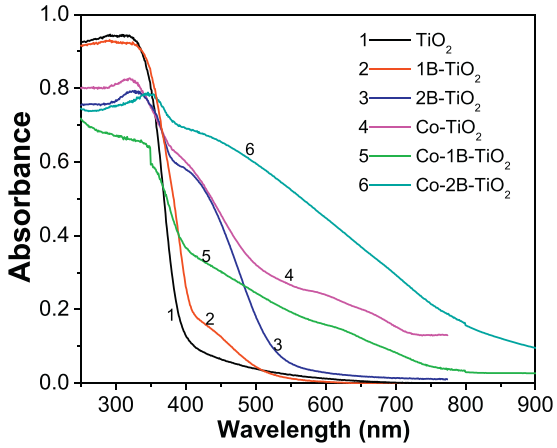

Fig. 8. UV–vis spectra of pure TiO_2, 1B–TiO_2, 2B–TiO_2, Co–TiO_2, Co–1B–TiO_2 and Co–2B–TiO_2.

and 2.57 eV above the valence band maxima (VBM) in the band gap and are separated by 0.33 eV. These electronic states explain the two step optical transition observed in the absorption spectra of the 2B–TiO_2 where B is in interstitial as well as substitutional sites as confirmed by XPS results. Unlike TiO_2–B_{int}, the energy states due to the interstitial B in $B_{int+sub}$ are found in the CB which overlap with the substitutional B states around E_F. The absence of shallow level in TiO_2–$B_{int+sub}$ near the conduction band minima(CBM) due to B_{int} is mainly attributed to interaction between the B_{int} and B_{sub} as indicated by this overlapping of B orbitals. B atoms both at interstitial and substitutional sites also behave as n-type dopant in TiO_2. On the contrary, Co substituting Ti in the TiO_2 lattice acts as a p-type dopant. Co forms two separated quite narrow energy bands (Fig. 9d) below CB at 2.56 and 3.04 eV from VB (at Γ point) thus reducing the band gap to 2.56 eV from 2.9 eV (for pure TiO_2) consistent with UV–vis spectra of Co-doped TiO_2. Co atoms also form some impurity states in the VB region which shows bonding states between Co and O atoms in TiO_2–Co. Upon mixing Co in B_{int} and $B_{int+sub}$ the states due to Co are mainly changed as observed from Fig. 9e. Two well separated Co impurity states in TiO_2–Co at 2.56 and 3.04 eV now changed to a broad peak around 1.5 eV in TiO_2–Co–B_{int}. Strong hybridization between Co and Ti states are also seen in this case which was not present in Co–TiO_2. In addition the overlapping of O and Co states is reduced with the formation of Co distinct levels above the VB. This shows that the presence of interstitial B alters the interaction between Co and host elements. No interaction between B_{int} and Co states is observed thus preserving the shallow level below CB owing to hybridization between B_{int}, O and Ti as observed in TiO_2–B_{int}. All these features were able to reduce the band gap of TiO_2–Co–B_{int} as observed for Co–1B–TiO_2 photocatalyst. The change in Co states is found similar in TiO_2–Co–$B_{int+sub}$ (Fig. 9f) as observed in TiO_2–Co–B_{int}. The only difference detected in TiO_2–Co–$B_{int+sub}$ is that Co in this case interacts with B_{sub} in addition to interaction with Ti near E_F. This interaction does not cause significant variation in the position of two localized intermediate states in the band gap due to B_{sub}. Nevertheless, these states are now located much closer to the VBM at 1.03 and 1.31 eV (at Γ point) mainly due to the positive shift of VBM by the formation of Co state above VB. This explains the higher visible light absorption by TiO_2–Co–$B_{int+sub}$ as compared to all the other samples mainly attributed to the two optical transitions of lower energy.

The recombination of photogenerated charges can be qualitatively investigated by studying the radiative emission caused by the recombination processes. PL emission spectra (Fig. 10a) were recorded for all the six samples by exciting with the wavelength of 385 nm (matching the band edge of the TiO_2). In the visible range, three distinct emission peaks located at 425, 486 and 572 nm are recorded where the first peak is attributed to the relaxation of self trapped exciton localized on TiO_6 octahedral while the other two emission peaks are assigned to the intraband transition within the energy level traps or surface defects related to oxygen vacancies [40,41]. Thus these are the signature peaks for the recombination of charge carrier. The intensity of the peaks increases for Co–TiO_2, 2B–TiO_2, and Co–1B–TiO_2 as compared to that of pure TiO_2 with highest intensity observed for Co–1B–TiO_2 powder. Thus the amount of radiative recombination process increases for these samples. On the contrary, in 1B–TiO_2 and Co–2B–TiO_2 the intensity of the peak decreases suggesting the reduction in radiative recombination of charge carriers by trapping in the dopant sites. This shows that Co implements completely different effect upon codoping with 1B and 2B where former combination (Co–1B–TiO_2) provides negative outcome by increasing the recombination processes as compared to 1B–TiO_2, while in later case the charge separation improves significantly. Tentatively the above result can be explained on the basis of interaction between Co and B. The states formed by Co element in TiO_2 always act as the recombination sites as observed from the Co–TiO_2 and also reported by Sadanandam et al. and Miao et al. [42,43]. In the above DFT studies it was seen that there was no interaction between Co and B_{int} when simulated for Co–1B–TiO_2 (Fig. 9e) photocatalyst and thus Co provides a recombination site in this case. While simulating Co–2B–TiO_2 structure using the DFT it was seen that the B_{sub} levels overlap with Co states indicating some hybridization between Co and B (Fig. 9f). This interaction might reduce the effect of Co, in Co–2B–TiO_2, responsible for recombination of charge carriers. In order to determine the lifetime of charge carriers, time resolved PL (TRPL) spectra (Fig. 10b) were acquired for all the six samples. The experimental TRPL intensity decay ($I(t)$) curve was fitted by the following multi-exponential equation:

$$I(t) = I_0 \sum_i \alpha_i e^{\frac{-t}{\tau_i}}$$

where the coefficients α_i are the pre-exponential factors and the decay times τ_i characterize the fluorescence decay of the i component of the mixture. The pre-exponential coefficients are related to the fractional contributions f_i of the total fluorescence emitted by the i-component of the mixture. The equation used determines the pre-exponential coefficients α_i, the fractional contributions f_i and the decay times τ_i up to four components.

$$f_i = \frac{\alpha_i \tau_i}{\sum_i \alpha_i \tau_i}$$

The average lifetime (Table 2) obtained for pure TiO_2 is around 1.49 ns which is comparable to that reported in the literature [44]. The lifetime value decreases for Co–TiO_2 and 2B–TiO_2 to 1 ns and 1.17 ns indicating fast recombination of charge carriers. However, the lifetimes recorded for 1B-TiO_2, Co–1B–TiO_2 and Co–2B–TiO_2 show the increase with highest value of 2.29 ns obtained for Co–2B–TiO_2. Both these results of PL show that upon codoping with Co–2B–TiO_2 the PL intensity as well as the time period for charge separation are improved, which are very promising for the photocatalytic reactions. The photocatalytic activity of all the six samples for degradation of *p*-NP and RhB dye are presented in Fig. 11a and b respectively. Under light irradiation, all the doped TiO_2 samples were able to degrade the pollutant much faster than the pure TiO_2 sample. Among all the samples Co–2B–TiO_2 showed the best activity, with 92 % and 95 % degradation of *p*-NP and RhB in 4 h and 2 h respectively. The degradation rate of Co–2B–TiO_2 is 7.8 and 3.3 times higher as compared to pure TiO_2 for *p*-NP and RhB dye degradation respectively. Both the B-doped TiO_2 showed bet-

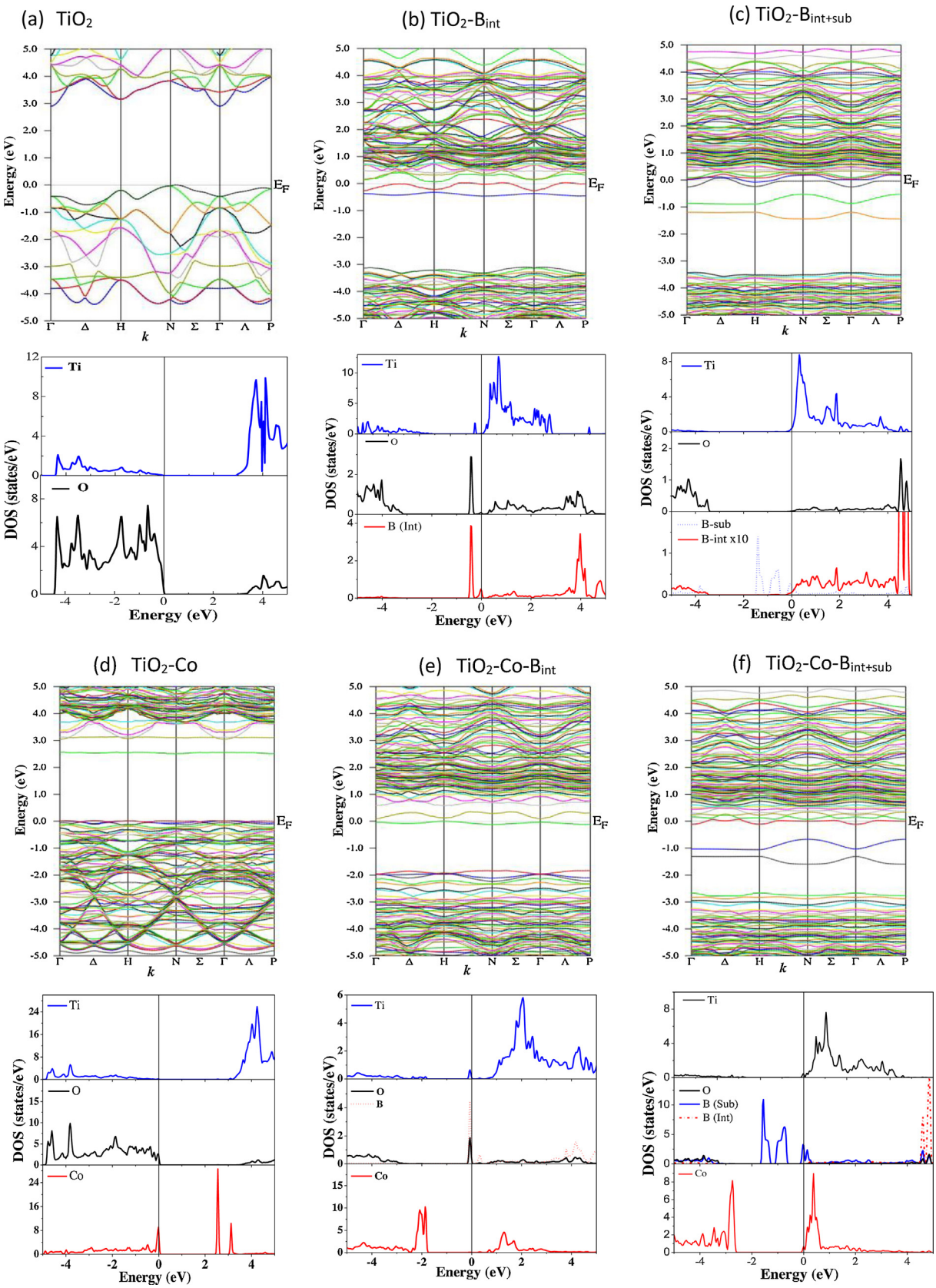

Fig. 9. Energy bands (upper panel) and partial density of states (PDOS) (lower panel) of (a) pure TiO_2, (b) TiO_2–B_{int}, (c) TiO_2–$B_{int+sub}$, (d) TiO_2–Co, (e) TiO_2–Co–B_{int}, and (f) TiO_2–Co–$B_{int+sub}$.

Table 2
Average life-time of charge carriers of pure TiO_2, 1B–TiO_2, 2B–TiO_2, Co–TiO_2, Co–1B–TiO_2 and Co–2B–TiO_2 obtained by fitting the time-resolved PL decay curve by two or three exponential components. Intensity fractions of these components are also reported.

Sample name	Life time			Intensity fraction			Average life time τ (ns)
	τ1 (ns)	τ2 (ns)	τ3 (ns)	f1	f2	f3	
TiO_2	2.95	0.829		0.31	0.69		1.49
1B–TiO_2	2.96	0.734		0.4	0.6		1.63
2B–TiO_2	2.49	0.599		0.299	0.701		1.17
Co–TiO_2	0.998	0.191	4.59	0.598	0.328	0.0746	1
Co–1B–TiO_2	1.28	0.331	5.79	0.369	0.425	0.206	1.81
Co–2B–TiO_2	1.28	0.171	7.88	0.249	0.512	0.24	2.29

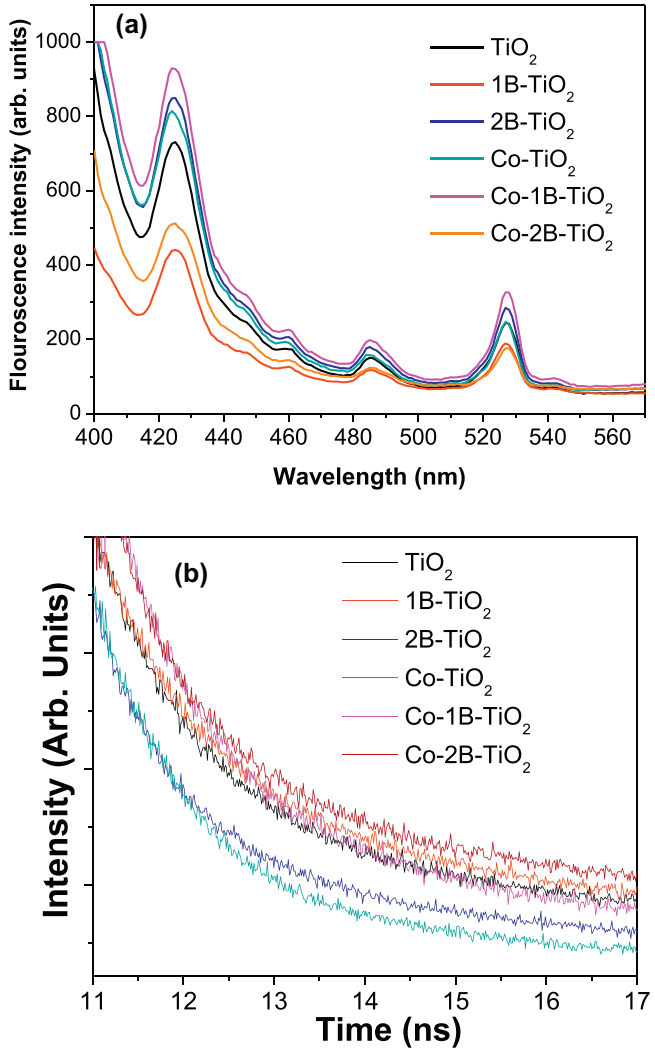

Fig. 10. (a) Photoluminescence emission spectra and (b) Time-resolved photoluminescence decay curve of pure TiO_2, 1B–TiO_2, 2B–TiO_2, Co–TiO_2, Co–1B–TiO_2 and Co–2B–TiO_2.

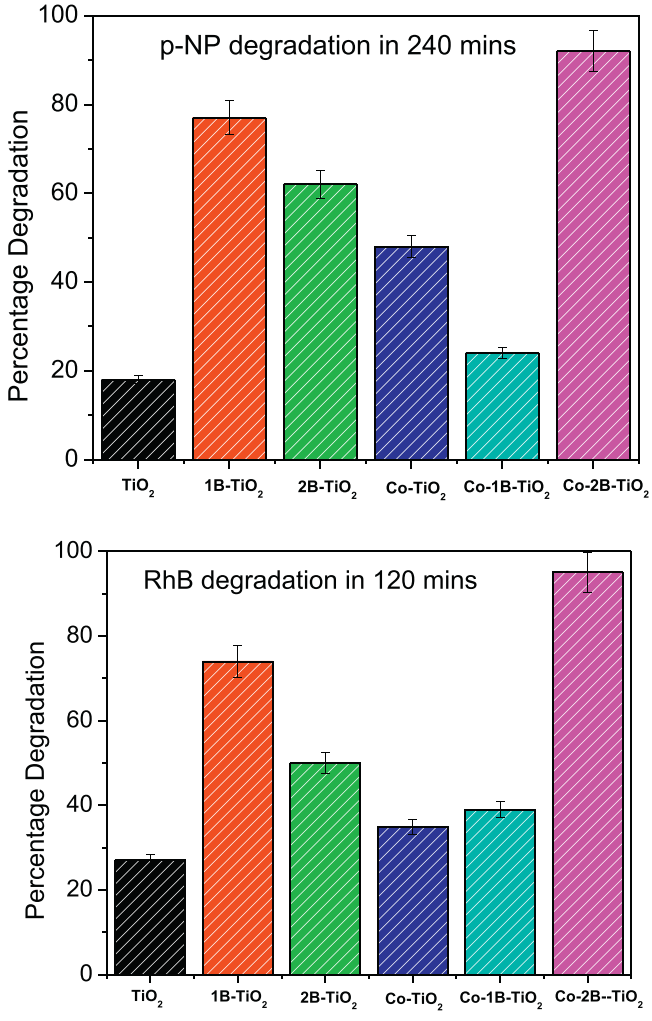

Fig. 11. Percentage degradation of (a) *p*-nitrophenol and (b) rhodamineblue dye in 4 h and 2 h under light irradiation, respectively, of pure TiO_2, 1B–TiO_2, 2B–TiO_2, Co–TiO_2, Co–1B–TiO_2 and Co–2B–TiO_2. Percentage degradation is obtained by measuring normalized intensity of the absorption band of *p*-NP and RhB at 320 nm and 550 nm, respectively, in UV–vis spectra with respect to time.

ter performance than Co-doped TiO_2 with 1B–TiO_2 being the best in mono-doped TiO_2. However, when Co is codoped with 1B the photocatalytic activity decreases drastically as compared to that for 1B–TiO_2. On the contrary for Co–2B–TiO_2 sample the codoping of Co and B improves the photocatalytic activity; for which it was observed that the degradation rates increase by 2.1 and 1.9 times as compared to that of 2B–TiO_2 for degrading *p*-NP and RhB respectively.

The recombination of photogenerated charges, visible light absorption capability, and the surface area of the photocatalyst are the three main factors controlling the photocatalytic activity. The surface area of all the doped TiO_2 samples is noticeably higher than that of pure TiO_2 samples. Although Co–1B–TiO_2 has the highest surface area (108.1 m^2/g) the activity is the lowest among the doped-TiO_2. Thus in the present case the surface area is not the main feature affecting the activity of the TiO_2, though it cannot be neglected. In B-doped TiO_2, the activity of 1B–TiO_2 is maximum and as the B concentration increases the activity decreases. No major variation is observed in the band gap of 1B–TiO_2. Therefore, in this case the enhanced activity is attributed to the reduced recombination processes (as confirmed by PL results) due to the formation of shallow level, below the CBM, of B—O—Ti bond which acts as

the trapping sites for the photogenerated electrons owing to the presence of Ti^{3+} in the bond. At higher B concentrations (2 at.% and 3 at.%), deep levels are formed by the B_{sub} which do not trap the photogenerated charges, but considerably enhance the visible light absorption capability which is responsible for higher activity. In the samples with higher B concentration, a shallow level does not get formed even by interstitial B because of the interaction between B_{sub} and B_{int} states. In the case of Co doping, the recombination rates are always high and caused by the formation of Co states in the band gap. Thus even if band gap is reduced the activity is low for all the Co–doped TiO_2 except for very low concentration of Co (0.1 at.%). Such a low concentration of Co might not contribute in recombination process but can certainly participate in the visible light absorption to improve the photocatalytic activity. When this small concentration of Co (0.1 at.%) is added to 1B– and 2B–TiO_2, two opposite effects were observed. In the case of Co–1B–TiO_2, the effectiveness of B_{int} in charge separation process by trapping electrons at B—O—Ti level gets hampered by the addition of Co. This negative effect is responsible in decreasing the activity in Co–1B–TiO_2 even though the visible light absorption is higher than that of 1B–TiO_2. On the contrary, the photocatalytic activity is considerably improved by adding a small amount of Co in 2B–TiO_2. The highest visible light absorption was achieved in Co–2B–TiO_2 due to the presence of deep intermediate levels of B_{sub} and positive shift of VBM by the formation of Co impurity levels. By improving the visible light absorption efficiency of TiO_2, a larger number of photogenerated charges can be formed which in turn would increase the degradation rate of pollutants. The lifetime of charge carriers was also found to be maximum for this sample, thus the photogenerated holes survive until they travel to the surface and participate in the photocatalytic degradation reaction. Both these features combine to produce synergic effect for photogeneration of charges, the charge separation, and the transfer of the charges to the surface for production of an oxidizing agent.

4. Conclusion

Codoping of TiO_2, a process which is expected to enhance the photocatalytic activity, might not be able to do so with an arbitrary choices of dopants and their concentrations. The present work was undertaken to find out the conditions necessary for the enhancement by exploitation of synergies between the increase in visible light absorption and the delay in the recombination of photogenerated charges. Our results show that codoping is necessary but not sufficient to enhance the photocatalytic activity of TiO_2. It is crucial to have a right combination of: (a) the type of dopants, (b) the concentration of dopants with appropriate lattice locations, and (c) appropriate interactions between the dopants. Lattice location of B in TiO_2 was tuned to determine its effect on the photocatalytic activity of Co–B codoped TiO_2. At low concentration of B-doping (1 at.%), B occupies the interstitial site as elucidated by XPS analysis. As the B concentration increases (2 at.% and 3 at.%), the dopant also occupies substitutional O position. With both of these B lattice locations in TiO_2, an improved photocatalytic activity is observed. This result is attributed to the effective charge separation obtained by the TiO_2–B_{int} shallow energy level; while higher visible light absorption is achieved with TiO_2–$B_{int+sub}$ owing to the presence of two deep energy levels in the band gap as confirmed by DFT calculations as well as by UV–vis absorption spectra. In the case of Co doping, the band gap of TiO_2 decreases but the recombination rates are always high, caused by the formation of Co impurity levels in the band gap. In this case, the photocatalytic activity is low for all the Co-doped TiO_2, except for a low concentration of Co (0.1 at.%). Two opposite effects were observed when small amount of Co (0.1 at.%) is codoped with B_{int} or $B_{int+sub}$. In particular, the photocatalytic degradation rate of organic aqueous pollutants (*p*-nitrophenol and rhodamine B dye) reduces for TiO_2–Co–B_{int} whereas it is enhanced remarkably for TiO_2–Co–$B_{int+sub}$ as compared to monodoped (∼2.1 times) and undoped (∼7.8 times) TiO_2. Higher photocatalytic activity observed in the codoped sample, with B both in interstitial and substitutional positions, is attributed to the interaction of Co with B at two different positions in TiO_2 lattice, which is able to produce synergistic effects by higher visible light absorption and improved charge separation.

Acknowledgements

The research activity is partially supported by UGC-UPE Green Technology Project in India and by the PAT (Provincia Autonoma di Trento) project ENAM in cooperation with Istituto PCB of CNR (Italy). One of us (AD) is thankful to DST New Delhi, India for INSPIRE Faculty Project. We thank N. Bazzanella for SEM analysis. R.S. Varma is thankful to WOS-A, DST New Delhi, India for Women Scientist Project. R. Fernandes acknowledges UGC, India for providing financial support through Dr. D.S. Kothari post-doctoral fellowship programme.

References

[1] X. Fujishima, X. Zhang, C. R. Chim. 9 (2006) 750–760.
[2] A. Zaleska, Recent Pat. Eng. 2 (2008) 157–164.
[3] W.Y. Choi, A. Termin, M.R. Hoffmann, J. Phys. Chem. 84 (1994) 13669–13679.
[4] M.I. Litter, J.A. Navio, J. Photochem. Photobiol. A Chem. 98 (1996) 171–181.
[5] R. Dholam, N. Patel, A. Santini, A. Miotello, Int. J. Hydrogen Energy 35 (2010) 9581–9590.
[6] R. Lopez, R. Gomez, M.E. Llanos, Catal. Today 148 (2009) 103–108.
[7] R. Dholam, N. Patel, M. Adami, A. Miotello, Int. J. Hydrogen Energy 34 (2009) 5337–5346.
[8] Miguel Pelaez, Nicholas T. Nolan, Suresh C. Pillai, Michael K. Seery, Polycarpos Falaras, Athanassios G. Kontos, Patrick S.M. Dunlop, Jeremy W.J. Hamilton, J. Anthony Byrne, Kevin O'shea, Mohammad H. Entezari, Appl. Catal. B: Environ. 125 (2012) 331–349.
[9] Swagata Banerjee, Suresh C. Pillai, Polycarpos Falaras, Kevin E. O'shea, John A. Byrne, Dionysios D. Dionysiou, J. Phys. Chem. Lett. 5 (2014) 2543–2554.
[10] W. Zhu, X. Qiu, V. Iancu, X.Q. Chen, H. Pan, W. Wang, N.M. Dimitrijevic, T. Rajh, H.M. Meyer III, M.P. Paranthaman, G.M. Stocks, H.H. Weitering, B. Gu, G. Eres, Z. Zhang, Phys. Rev. Lett. 103 (2009) 226401–226404.
[11] Y. Gai, J. Li, S.S. Li, J.B. Xia, S.H. Wei, Phys. Rev. Lett. 102 (2009) 0364021–0364024.
[12] Y. Cong, J.L. Zhang, F. Chen, M. Anpo, J. Phys. Chem. C 111 (2007) 6976–6982.
[13] R. Jaiswal, N. Patel, D.C. Kothari, A. Miotello, Appl. Catal. B Environ. 126 (2012) 47–54.
[14] N. Patel, R. Jaiswal, T. Warang, G. Scarduelli, A. Dashora, B.L. Ahuja, D.C. Kothari, A. Miotello, Appl. Catal. B Environ. 150 (2014) 74–81.
[15] A. Dashora, N. Patel, D.C. Kothari, B.L. Ahuja, A. Miotello, Sol. Energy Mater. Sol. Cells 125 (2014) 120–126.
[16] R. Jaiswal, J. Bharambe, N. Patel, D.C. Kothari, A. Miotello, Appl. Catal. B Environ. 168 (2015) 333–341.
[17] W.C. Lu, H.D. Nguyen, C. Yi Wu, K.S. Chang, J. Appl. Phys. 115 (2014) 144305–1443051.
[18] S. Zhang, Ultrason. Sonochem. 19 (2012) 767–771.
[19] Gai J. Li, S.S. Li, J.B. Xia, S.H. Wei, Phys. Rev. Lett. 102 (036402) (2009) 1–4.
[20] Y. Wu, J. Zhang, L. Xiao, F. Chen, Appl. Surf. Sci. 256 (2010) 4260–4268.
[21] N. Feng, A. Zheng, Q. Wang, P. Ren, X. Gao, S.B. Liu, Z. Shen, T. Chen, Feng Deng, J. Phys. Chem. 115 (2011) 2709–2719.
[22] C. Sun, D.J. Searles, J. Phys. Chem. C 117 (2013) 26454–26459.
[23] S. In, A. Orlov, R. Berg, F. García, Sergio P. Jimenez, M.S. Tikhov, D.S. Wright, R.M. Lambert, J. Am. Chem. Soc. 129 (2007) 13790–13791.
[24] G. Liu, C. Sun, L. Cheng, Y. Jin, H. Lu, L. Wang, S.C. Smith, G.Q. Lu, H.M. Cheng, J. Phys. Chem. C 113 (2009) 12317–12324.
[25] W. Zhao, W. Ma, C. Chen, J. Zhao, Z. Shuai, J. Am. Chem. Soc. 126 (2004) 4782–4783.
[26] T. Tokmakci, A. Ozturk, J. Park, Ceram. Int. 39 (2013) 5893–5899.
[27] M. Bettinelli, V. Dallacasa, D. Falcomer, P. Fornasiero, V. Gombac, T. Montini, L. Roman'o, A. Speghini, J. Hazard. Mater. 146 (2007) 529–534.
[28] R. Khana, S.W. Kima, T.J. Kima, C.M. Namb, Mater. Chem. Phys. 112 (2008) 167–172.
[29] S. Bagwasi, B. Tian, J. Zhang, M. Nasir, Chem. Eng. J. 217 (2013) 108–118.
[30] X. Lan, L. Wang, B. Zhang, B. Tian, J. Zhang, Catal. Today 224 (2013) 163–170.
[31] E. Finazzi, C.D. Valentin, G. Pacchioni, J. Phys. Chem. C 113 (2009) 220–228.
[32] K. Yang, Y. Dai, B. Huang, J. Phys. Chem. C 114 (2010) 19,830–19834.
[33] A. Zaleska, E. Grabowska, J.W. Sobczak, M. Gazda, J. Hupka, Appl. Catal. B: Environ. 89 (2009) 469–475.

[34] P. Blaha, K. Schwarz, J. Luitz, Wien2K Code, An Augmented Plane Wave Plus Local Orbitals Program for Calculating Crystal Properties, Vienna University of Technology, Vienna, Austria, 2001.
[35] J.P. Perdew, A. Ruzsinszky, G.I. Csonka, O.A. Vydrov, G.E. Scuseria, L.A. Constantin, X. Zhou, K. Burke, Phys. Rev. Lett. 100 (136406) (2008) 1–4.
[36] F. Tran, P. Blaha, Phys. Rev. Lett. 102 (226401) (2009) 1–4.
[37] A. Rubio-Ponce, A. Conde-Gallardo, D. Olguín, Phys. Rev. B 78 (035107) (2008) 1–9.
[38] N. Patel, Alpa Dashora, R. Jaiswal, R. Fernandes, M. Yadav, D.C. Kothari, B.L. Ahuja, A. Miotello, Phys. Chem. C 119 (2015) 18581–18590.
[39] D.A.H. Hanaor, C.C. Sorrell, J. Mater. Sci. 46 (2011) 855–874.
[40] S. Chen, W. Chu, Y.Y. Huang, X. Liu, D.G. Tong, Mater. Res. Bull. 47 (2012) 4514–4521.
[41] R. Chauhan, A. Kumar, R.P. Chaudhary, Spectrochim. Acta Part A: Mol. Biomol. Spectorsc. 98 (2012) 256–264.
[42] G. Sadanandam, K. Lalitha, V.D. Kumari, M.V. Shankar, M. Subrahmanyam, Int. J. Hydrogen Energy 38 (2013) 9655–9664.
[43] Y. Miao, Z. Zhai, L. Jiang, Y. Shi, Z. Yan, D. Duan, K. Zhen, J. Wang, Powder Technol. 266 (2014) 365–371.
[44] B. Choudhary, A. Choudhary, J. Lumin. 136 (2013) 339–346.